Chemical Engineering Journal 463 (2023) 142512

Contents lists available at ScienceDirect

Chemical Engineering Journal

journal homepage: www.elsevier.com/locate/cej

Efficient photosynthesis of H_2O_2 via two-electron oxygen reduction reaction by defective g-C_3N_4 with terminal cyano groups and nitrogen vacancies

Jiaoni Li [a], Jinhui Huang [a,*], Guangming Zeng [a,*], Chenyu Zhang [a], Hanbo Yu [b,c], Qiongfang Wan [a], Kaixin Yi [a], Wei Zhang [a], Haoling Pang [a], Si Liu [a], Suzhou Li [a], Wenjuan He [a]

[a] *College of Environmental Science and Engineering, Hunan University, Changsha 410082, China*
[b] *School of Hydraulic and Environmental Engineering, Changsha University of Science & Technology, Changsha 410114, China*
[c] *Key Laboratory of Dongting Lake Aquatic Eco-Environmental Control and Restoration of Hunan Province, Changsha 410114, China*

ARTICLE INFO

Keywords:
Graphitic carbon nitride
Photocatalytic H_2O_2 generation
N defects
Oxygen reduction reaction
Internal electric field

ABSTRACT

The development of photocatalysts for the efficient generation of hydrogen peroxide (H_2O_2) and degradation of antibiotic pollutants is a mutual-beneficial solution to the chemical resource demands and environmental remediation. Herein, efficient visible-light-driven H_2O_2 production and antibiotic degradation are achieved by using nitrogen-deficient modified polymeric carbon nitride (g-C_3N_4) to facilitate the reduction of dioxygen. The N defects modified g-C_3N_4 reached an excellent H_2O_2 generation rate of 623.5 μmol $g^{-1}h^{-1}$ without O_2 bubbling. The structural features and entire photocatalytic conversion process were systematically studied via experiments and theoretical calculations. It was found that the N defects in the framework constructed a giant internal electric field (IEF), which effectively inhibited carrier recombination. Revealed the neglected H_2O_2 production via $^1O_2$ pathway, which effectively promoting the selective $2e^-$ oxygen reduction reaction (ORR). More interestingly, the N defects structure greatly improved the O_2 adsorption ability and O_2 production ability of the material, while inhibiting the in situ generated H_2O_2 from being decomposed and maintaining high efficiency of H_2O_2 production under air conditions. This study thoroughly revealed the synergistic effects of the terminal cyano group and nitrogen vacancies over g-C_3N_4 for efficient H_2O_2 photogeneration photosynthesis.

1. Introduction

Hydrogen peroxide (H_2O_2) is considered as a potential clean and high-energy oxidant, which is widely applied in electronic industries, pulp bleaching, textile industry, and detergent industry [1–4]. Particularly in the field of environmental protection, H_2O_2 is utilized in advanced oxidation processes (AOPs) to generate reactive species (•OH, •OOH) for pollutant degradation, surface soil remediation, and water disinfection [5–8]. However, the traditional H_2O_2 production methods, such as the anthraquinone method, have severe shortcomings. Examples include highly energy-consuming or complex industrial processes [9–11]. Photocatalysis, the most economical and cleanest method to generate H_2O_2, has received increasing attention in recent years [12–15]. The photosynthesis of H_2O_2 adhere to the basic principle of photocatalysis. Generally, oxygen in aqueous solution is reduced to H_2O_2 via a two-electron pathway ($O_2 + 2H^+ + 2e^- \rightarrow H_2O_2$, $E = 0.68$ V_{NHE}) [16,17]. This reaction competes with the four-electron pathway ($O_2 + 4H^+ + 4e^- \rightarrow 2H_2O$), which is more exergonic thermodynamically than the $2e^-$ pathway. In this regard, developing novel photocatalysts with a higher degree of selectivity and cost-effectiveness for $2e^-$ oxygen reduction reaction (ORR) is still a critical challenge [13,18].

The graphite carbon nitride (g-C_3N_4), a semiconductor with low-cost and non-metal properties, exhibits giant application potential in the research of H_2O_2 generation [19,20]. Since the splitting of water requires overcoming a huge energy barrier, the reactions are usually carried out in the presence of alcohols as sacrificial agents [20]. Such as ethanol, photoexcitation on the surface of the material generates holes to oxidize the alcohol and produce aldehydes and protons, while e^- promotes the two-electron reduction of O_2 and produces H_2O_2 [21]. Several g-C_3N_4 catalysts modified with organic semiconductors such as aromatic diamines or loaded with Au or Au-Ag alloy nanoparticles have been proposed [22]. However, most of them exhibit poor selectivity for

---

* Corresponding authors at: College of Environmental Science and Engineering, Hunan University, Changsha 410082, China.
E-mail addresses: huangjinhui_59@163.com (J. Huang), zgming@hnu.edu.cn (G. Zeng).

https://doi.org/10.1016/j.cej.2023.142512
Received 27 October 2022; Received in revised form 27 February 2023; Accepted 17 March 2023

the two-electron oxygen reduction of H_2O_2. This may be related to the pathway of H_2O_2 generation. In most of the studies, the single electron reduction of O_2 is dominant and generates superoxide radicals. The H_2O_2 is generated by the superoxide radical pathway. The loss of electrons may exist in this two-step reduction process. Inhibiting the selective two-electron oxygen reduction to produce H_2O_2 [21]. In addition, another reason for the low H_2O_2 selectivity is that the H_2O_2 formed in situ may occupy the reactive site and decomposed by reacting with the CB electrons and VB holes of the material. Further affects the total yield of H_2O_2. It can be seen that efficient H_2O_2 production requires selective promotion of the two-electron reduction of O_2 and inhibition of the photodecomposition of the subsequently formed H_2O_2.

More important, the photocatalytic performance of the material is a major influencing factor for the selective reduction of H_2O_2 production. The rapid recombination of electron-hole pairs generated by photoexcitation inhibits the production of H_2O_2. The introduction of structural defects into the g-C_3N_4 plane, such as surface groups and vacancies, has been embraced as an efficient technique for considerably increasing photocatalytic activity [23–25]. The vacancies created in g-C_3N_4 can act as extra reactive sites to catalyze surface photoreactions more efficiently [24]. In addition, the crystallinity of g-C_3N_4 can be greatly affected while constructing vacancies, which significantly affects the photocatalytic performance and limits the application dramatically. Introducing novel functional groups inside the frameworks with g-C_3N_4 can modify the electronic structure and make the local electrostatic potential differences stronger [26–28]. More significantly, this change is similar to semiconductors with an internal electric field (IEF). The IEF facilitates charge transport and separation, which improves the photocatalytic ability even more [26,27,29,30]. Therefore, the introduction of functional groups based on the conventional vacancy defects is a feasible method to improve the photocatalytic efficiency.

Herein, the g-C_3N_4 with rich N vacancies and cyano groups (denoted as Nv-M) was fabricated through facile urea polymerization utilizing KOH to modify the carbon nitride framework. The theoretical calculations demonstrated how the introduction of N vacancy and cyano group induces an uneven charge distribution while regulating the energy band structure. Such unique phenomena further promote the formation of IEF steering charge migration and separation, which significantly improves the photocatalytic performance. However, studies on IEF for N defects g-C_3N_4 have mostly stayed in theoretical calculations [31,32]. Here we further show the effect of introducing N defects on the IEF of the g-C_3N_4 in combination with characterization and Kanata model. It has been demonstrated that the enhanced adsorption ability of O_2 directly contributes to the photocatalytic ORR, and the possible reaction pathways for photocatalytic H_2O_2 production were proposed subsequently. After activation by visible light under air condition, the as-prepared photocatalysts successfully oxidize water and maintain high selectivity for $2e^-$ ORR. There are many studies on the production of H_2O_2 by the $\bullet O_2^-$ pathway, the production of H_2O_2 by the $^1O_2$ pathway is less [33,34]. Most of them stay at the level of theoretical calculations, and the reaction mechanism is still unclear [34]. Here, we propose a possible pathway to produce H_2O_2 from $^1O_2$. O_2 directly produces $^1O_2$ via the energy transfer pathway, and $^1O_2$ produces H_2O_2 via two-electron reduction. Meanwhile, the introduction of N defects in the modified material effectively inhibits the in situ decomposition of H_2O_2. The two-electron oxygen reduction selectivity of H_2O_2 was further enhanced. Furthermore, the photogenerated holes (h^+) oxidize water to produced O_2 and protons, while the electrons (e^-) accelerate the $2e^-$ reduction of O_2 which further enhanced the photocatalytic performance under visible irradiation. Subsequently, we assessed the efficacy of the Nv-M photo-generated $\bullet O_2^-$ and $^1O_2$ for water decontamination using tetracycline (TC, a common broad-spectrum antibiotic used globally) as a model organic molecule [8,35,36]. Combined with the photodegradation experiment, the presence of the generated ROS were further confirmed, which broadened the application of the as-prepared Nv-M photocatalysts in environmental remediation.

2. Experimental section

2.1. Photocatalysts preparation

The synthesis of primitive g-C_3N_4 (PCN): the primitive g-C_3N_4 was synthesized according to the reported method [37]. Briefly, carry 15 g of urea in a lidded crucible, and then calcined for 2 h at 550 °C in a muffle furnace under air condition. The heating rate used in this case was 10 °C min^{-1}.

The synthesis of Nv-M: 15 g of urea and a certain weight of KOH were dissolved in 30 mL deionized water and dried at 80 °C for 16 h until complete evaporation. The solid product was then put into the lidded crucible and calcined at 550 °C for 2 h. The experimental conditions were consistent with the primitive material. The product was then rinsed with deionized water and ethanol alternately to eliminate the remaining alkali. The samples with different KOH usage (0.01, 0.05, 0.1, 0.2 g) added were represented by Nv-M (M is the amount of KOH).

2.2. Photocatalytic reduction of O_2 to H_2O_2

Typically, 50 mg of material (1 g L^{-1}) was dispersed in 45 mL pure water and 5 mL isopropanol (IPA). Then the reaction was carried out for 30 min under dark conditions to completely disperse catalyst powder and ensure the adsorption–desorption equilibrium among the catalyst, dissolved oxygen, and solution. After that, the photoreaction test was started by irradiating reaction solution with a 300 W Xenon lamp ($\lambda \geq$ 420 nm, 40 mW cm^{-2}). In the light illumination process, 0.5 mL of sample was taken at the given time interval. Then the samples were filtered through Millipore filters (0.45 μm) to separate the materials. To further explore how H^+ concentration affects the reaction, the pH of the reaction solution was adjusted by $HClO_4$ and KOH. The concentration of the H_2O_2 was determined by iodometry method [2]. The total amount of H_2O_2 produced during the reaction can be calculated from the absorbance at 350 nm measured by UV–vis spectroscopy.

Additionally, the quenching experiment has been performed to explore the role of the reactive species. In a typical trial, various 2 mM of scavengers, including $AgNO_3$, EDTA-2Na, TEMPOL, L-tryptophan, and 1 mL methanol, were individually added into the reaction process for trapping electron (e^-), hole (h^+), superoxide radical ($\bullet O_2^-$), singlet oxygen ($^1O_2$), and hydroxyl radical ($\bullet OH$), respectively. The influence of different gases (N_2 or O_2) on the photocatalytic generation activity of H_2O_2 was discussed. First, continuously inject N_2 into the reaction solution under dark conditions for 60 min to ensure that no O_2 remains. Then the photocatalysis experiment was carried out under the condition of continuous N_2 flow.

2.3. Photocatalytic degradation of TC

In the model experiment, 100 mL of TC (20 mg mL^{-1}) aqueous solution was stirred with 50 mg of photocatalyst in the dark for 30 min, so that the balance of adsorption–desorption could be reached. Then the reactor was illuminated with the 300 W Xe lamp ($\lambda \geq$ 420 nm) under continuous stirring. At each time interval, 1 mL of the sample was taken and filtered through a 0.45 μm filter membrane. Finally, a UV–vis spectrophotometer was used to analyze the TC concentrations. The quenching experiment has been performed by added different quenching agents into the TC photodegradation experiments under the same conditions, the concentration of $AgNO_3$, EDTA-2Na, TEMPOL, L-tryptophan, catalase added to the reaction system were all 2 mM, and 1 mL methanol was added into the reaction system.

3. Results and discussion

3.1. Microscopic morphology and band structure of Nv–M

Nitrogen-deficient modified g-C_3N_4 was fabricated through a selective in-situ introduction of nitrogen defects via KOH-assisted urea at relatively high temperature by thermal polymerization. The molecular structure was shown in Fig. 1a, where a N vacancy and cyano group were introduced into the framework. Typical scanning electron microscopy (SEM) results for PCN and Nv-M are provided in Fig. 1b and S1, revealing similar irregularly curved layers and bulk-like structures. Notably, Nv-M becomes more fragmented due to the etching effect of KOH added during synthesis. Fig. 2a showed the N_2 physisorption measurements. The BET (Brunauer, Emmett and Teller) specific surface areas of PCN, Nv-0.05 and Nv-0.2 products were determined to be 86.42, 62.22, 22.31 m^2 g^{-1}, correspondingly. It was observed that the N defects modified Nv-M shows lowered surface area compared to the PCN. Furthermore, the specific surface area of the material is gradually reduced with the increased addition of KOH. This may be due to the fact that the addition of KOH destroyed the original structure of the material. This result can be further confirmed by combining the findings of SEM and FTIR. (Fig. 1b and 3a) The higher specific surface area does not necessarily ensure a higher H_2O_2 generation. The more reliable criteria of photocatalytic H_2O_2 generation performance was directly associated to O_2 adsorption capacity.

The light-harvesting ability and electrical performance of the as-fabricated material were directly determined by the bandgap and band edge [38]. Fig. S2 showed the UV–vis diffuse reflectance spectroscopy (DRS) spectra of PCN and Nv-M. The results showed that the DRS of Nv-M was progressive redshift with increasing KOH usage, and the color of samples changed from light yellow to dark. The intrinsic adsorption bands were significantly enhanced due to the $\pi \rightarrow \pi^*$ overlapping electronic transition in the sp^2-hybridized center in the aromatic ring of the conjugate. New adsorption bands might be originated from a lone pair of electrons on the defect sites. [39,40] The transformed Kubelka-munk function derived from Fig. S2 were shown in Fig. 2b, the bandgap energy progressively narrowed from 2.61 (PCN) to 2.46 (Nv-0.2) eV. From the respective XPS valence band (VB) spectra (Fig. S3), it can be inferred that PCN and Nv-M have the same VB edge energy. According to the formula: $E_{NHE}/\nu = \Phi + VB_{max} - 4.44$ (E_{NHE} is the potential of NHE; Φ is the electron work function of the analyzer, which is 3.88 eV; VB_{max} is 2.26 eV, which obtained from VB XPS spectra), the VB was calculated to be 1.70 eV relative to the NHE at pH 7 [41]. The obtained Mott–Schottky (M−S) plots with positive slopes suggested that PCN and Nv-M were typical n-type semiconductors (Fig. S4).

3.2. Structural characteristics of defects in Nv-M

The PCN and nitrogen-deficient modified g-C_3N_4 structures were investigated via X-ray diffraction (XRD) patterns. In Fig. 3a, all Nv-M samples showed two peaks at near 13.0° and 27.5°, nominated as (1 0 0) and (0 0 2) crystal planes [39,42]. The small shifts of (0 0 2) peak can be indexed to the stacking distance between nanosheets progressively smaller with increasing KOH usage. Furthermore, the characteristic (1 0 0) peaks in N_V-M were gradually attenuated, proposing that the etching effect of KOH influences the structure of g-C_3N_4. It may lead to a slight disruption of well-ordered structure in the framework and the creation of defects. Fig. 3b shows the Fourier transform infrared (FTIR) spectroscopy, which elucidates the molecular structure evolutions. Fig. 3b showed a typical characteristic peak of a heptazine ring at 808 cm^{-1}, confirming that a graphitic carbon nitride structure was formed. The stretched —N—C═N heterocycle gives rise to a strong band ranging from 900 to 1750 cm^{-1} [37,43]. Compared with PCN, the skeletal stretching model of Nv-M is unchanged during the evolutions, confirming that the material is still a heptazine unit structure. In addition, as

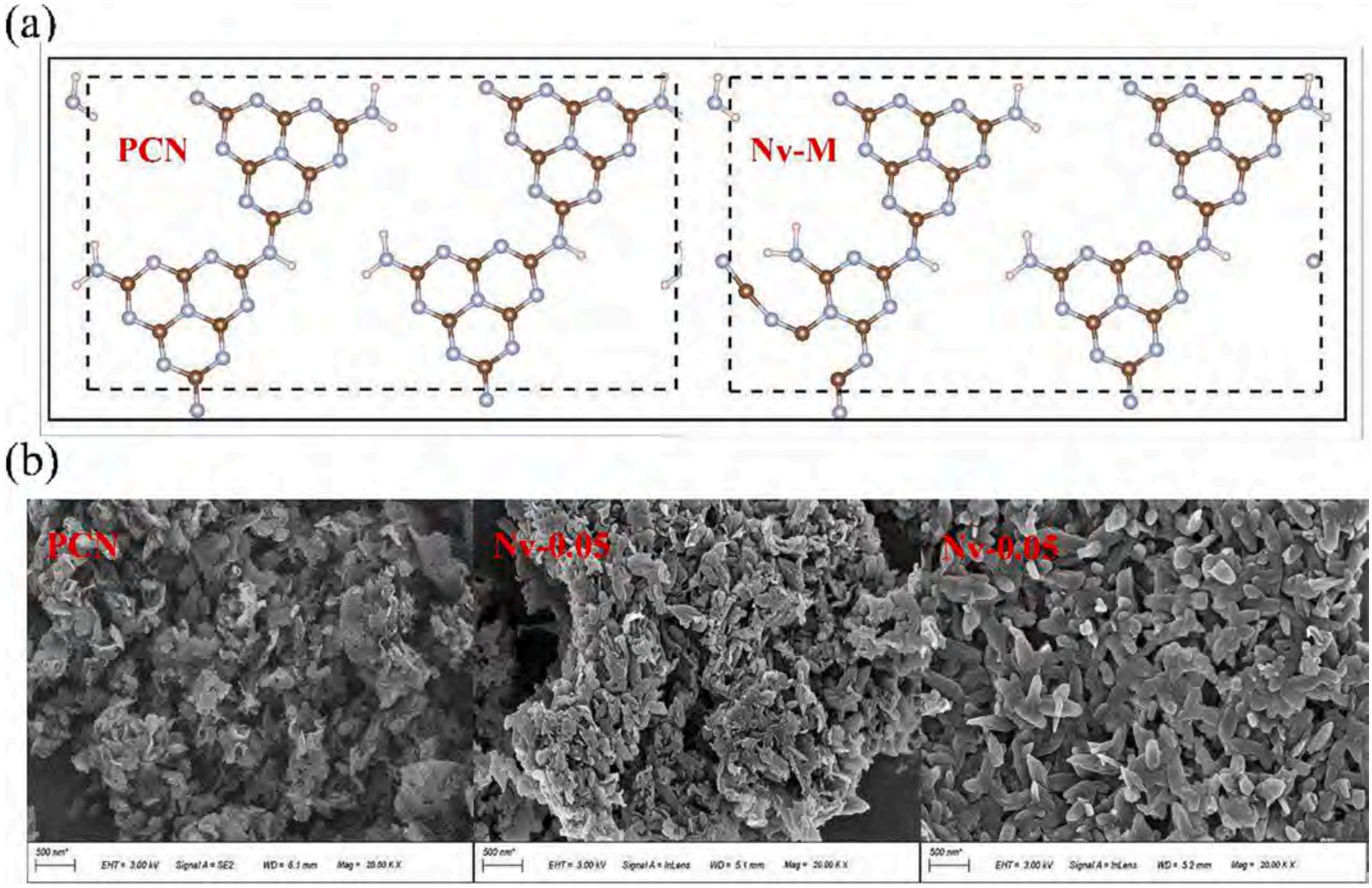

Fig. 1. (a) The structural modifications of PCN heptazine units introduce N defects. (b) The N defects induced modifications to the microscopic morphology (SEM) of PCN. The blue, brown, and pink spheres represent N, C, and H atoms, respectively.

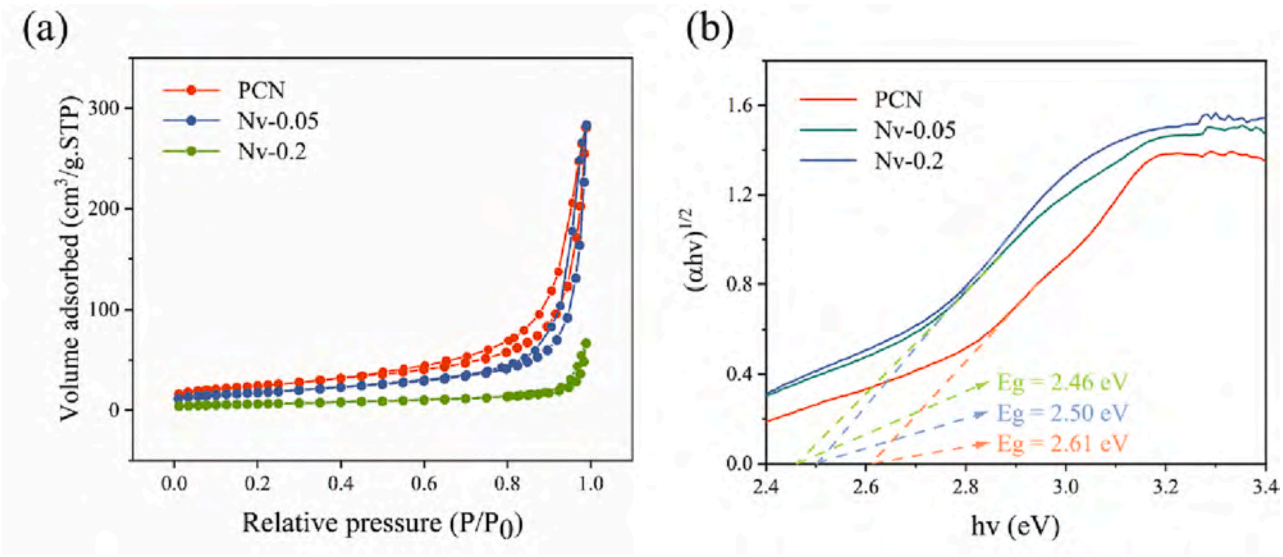

Fig. 2. (a) the isotherms of N_2 adsorption and desorption for PCN, Nv-0.05, and Nv-0.2. (b) Plots of the photon energy versus transformed Kubelka-Munk function for all samples.

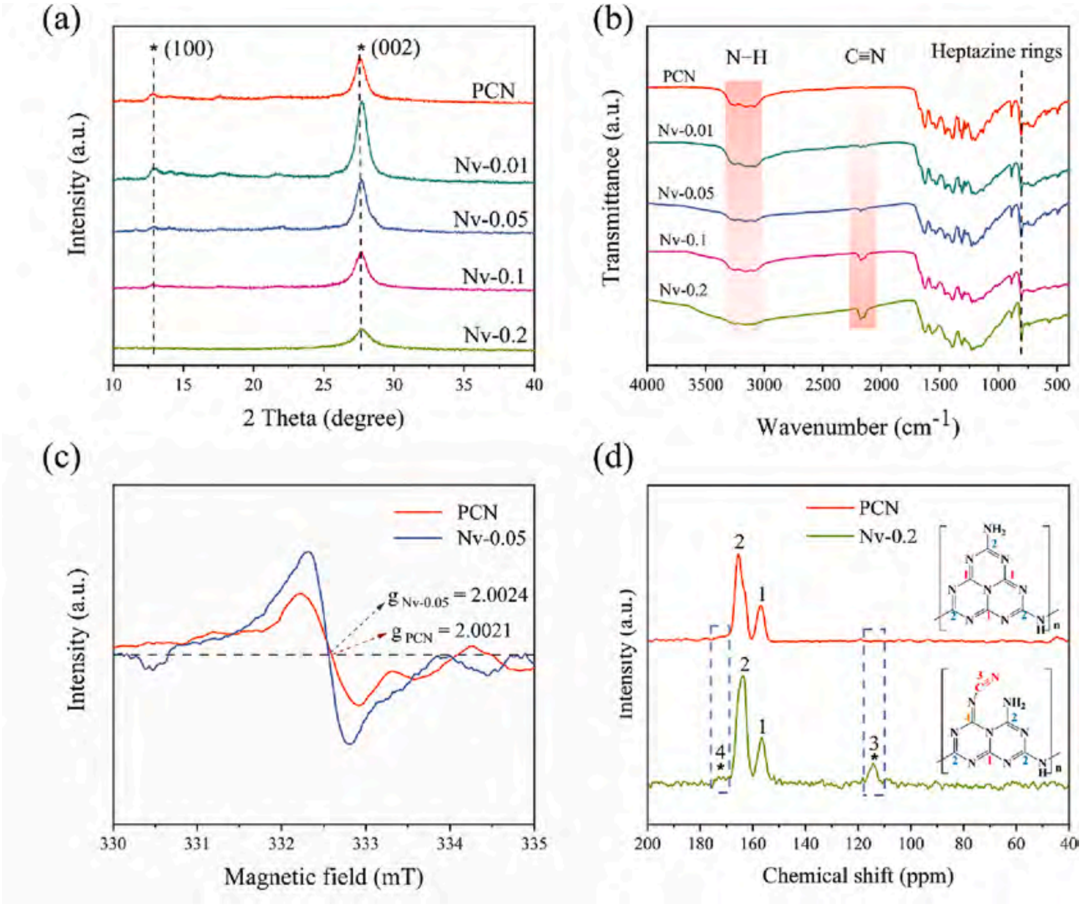

Fig. 3. (a) XRD patterns and (b) FTIR spectra of all samples. (c) The EPR spectra and (d) The solid-state 13C MAS NMR spectra of PCN and Nv-M.

shown in the highlighted red shaded area in Fig. 3b, two significant changes can be seen as the amount of KOH increase. Firstly, the strength of the N–H stretched vibrations gradually reduction in the interval from 3000 to 3350 cm^{-1} [37,39,43]. Second, the new peak was generated around 2174 cm^{-1}, which significantly derived from the asymmetric stretching vibrations of the cyano groups [37,39,43]. The peak intensity increases correspondingly with the increase in KOH usage, indicating that the modification reduced the density of the N–H group as well as the introduction of the cyano group. Electron paramagnetic resonance (EPR) further confirmed these results. In Fig. 3, considering the slight variation of γ during the experiment, it can be found that the centers of both Lorentzian lines are substantially the similar values of g (2.0021 for

PCN and 2.0024 for Nv-0.05). This indicated that PCN and Nv-M produced the same type of lone pair of electrons [44]. However, the intensity of Nv-0.05 is distinctly enhanced compared to PCN. This indicated that the density of the unpaired electrons in Nv-0.05 was higher than that of PCN [45]. The increased density of the unpaired electrons was mainly caused by the introduction of N vacancy in Nv-0.05. The loss of the N atoms from the aromatic ring of the modified material left extra electrons [46,47]. These extra electrons can be reassigned to the nearest C atom, resulting in a higher density of unpaired electrons [45,48]. Since Nv-0.05 introduced a strong electron-absorbing cyano group capable of delocalizing the lone pair of electrons in the π-conjugated heterocycle [44]. According to previous reports, such delocalization of π-conjugated heterocycles can facilitate the production of radicals, thereby improving the photocatalytic activity of the materials [29,44,45]. As shown in Fig. 3d, Solid-state ^{13}C magic angle spinning (NMR) was carried out to provide locations of the newly formed cyano group. The spectrum of both PCN and Nv-0.2 showed two intense vibrational peaks at 156.7 and 164.6 ppm, according to the C_{3N} (1) and C_{2N}–NH_X (2) of the heptazine ring, correspondingly [39,49] Furthermore, two new peaks around 172.3 and 114.1 ppm can be clearly found in Nv-0.2, which belong to the carbon atom (3) in cyano groups and the neighbor carbon atom (4), respectively [29,39,49]. Compared with PCN, the intensity ratio of peak (1) and peak (2) of Nv-0.2 changed from 1:2 to 1:2.27. Although not significant, the peak (1) related to C_{2N}–NH_X loses its strength with the addition of KOH over the course of Nv-M composition. According to the above results, the cyano group probably derived by deprotonating of –C–NH_X.

X-ray photoelectron spectroscopy (XPS) as a tool for determining the structure and elemental compositions of material surface. Table S1 showed the representative N/C and O/C ratio of atoms for the PCN and Nv-M surfaces. The results showed that the examined oxygen content was trace, which ruled out the feasibility of introducing a hydroxyl group in the structure of the synthesized Nv-M. The XPS survey spectra showed a slightly increasing trend of O 1 s peaks, which may be attributed to the higher O_2 adsorption capacity of the Nv-M (Fig. S5) [37]. The N/C ratio of atoms dropped considerably from 1.24 (PCN) to 0.90 (Nv–0.2). These results indicated that surface N defects were induced by KOH treatment. The C 1 s (Fig. 4a) and N 1 s (Fig. 4b) spectrums of PCN and Nv-M samples were collected to identify the introduced surface defects. The C 1 s spectra of PCN and Nv-M was presented in Fig. 4a. It can be seen that both Nv-M and PCN contained the same binding energy peaks at 284.8, 286.4, and 288.2 eV. These were attributed to the adventitious carbons, C–NH_x ($x = 1, 2$), and N–C = N in typical aromatic g-C_3N_4 heterocyclics, respectively [37,49]. The C1s spectrum of Nv-0.2 showed an intensified peak at 286.4 eV ascribing to the cyano group, which has the same energy as C–NH_x. The creation of a cyano group in Nv-M was further demonstrated by combining FTIR and NMR as previously discussed. The N1s XPS spectra of PCN contained three binding energy centered at 398.6, 400.2, and 401.3 eV. They referred to bi-coordinated N (N_{2C}), tri-coordinated N (N_{3C}), and amino N (–C–NH_X), respectively (Fig. 4b) [50,51]. The N_{3C} peaks changed from 400.2 to 399.6 eV, which exhibited a tendency to shift toward a low binding energy as the amount of KOH increased during thermal polymerization. This probably induced by the cyano group with a binding energy that lies between N_{2C} and N_{3C} (Table S2) [37]. Moreover, the N_{2C}/C atomic ratios of Nv-0.2 significantly decreased from 1.14 (PCN) to 0.88 (Nv-0.2), suggesting that N_{2C} defects were formed in Nv-M. As seen in Fig. S6a, the most stable geometry of Nv-M was determined by theoretically calculating the energies of the six potential models (M1–M6). The N_{2C} vacancies are preferentially designed in the vicinity of the cyano group, since the lower energy indicates a more stable structure (M6). The discovery shows a tendency for the cyano groups and the N vacancies to be close (Fig. S6b) [39,52].

3.3. *Carrier separation characteristics and internal electric field of Nv-M*

Besides visible-light absorption and band structure, the defective structure in Nv-M affects the separation and transport of photogenerated electron-hole. First, the charge density difference (Fig. 5a, b) for PCN and Nv-M were calculated to demonstrate whether N defects can improve the separation of photogenerated carriers. Fig. 5a demonstrated the positions of the highest occupied molecular orbital (HOMO) and the lowest unoccupied molecular orbital (LUMO) of PCN. Obviously, the density of charge states on the ring was equally distributed, owing to the high symmetric planar structures of PCN. In contrast, the charge density in Nv-M was redistributed, creating some electron-rich regions (Fig. 5b). That local charge accumulation caused the CB to move down [49]. In addition, the introduction of the N defects causes more localization of charge density distributions, resulting in the formation of high- and low-density regions of valence electrons, i.e., an IEF was constructed [53,54]. Such an induced IEF could promote separation of photogenerated carriers as well as reduced and oxidized sites, efficiently facilitating the reaction of electrons and holes on the surface [43,49,55]. The IEF intensity of the samples was measured using a model developed by Kanata [56,57]. The model demonstrates that the IEF intensity is determined by the surface potential and the surface charge density [54,58]. First, the zeta potential of the material in NaCl solution was measured (Fig. S20) The surface charge densities of Nv-0.05 and PCN were calculated according to the Gouy-Chapman model, as shown in Fig [58]. The surface potentials of the samples were obtained by atomic force microscopy surface (AFM) potential pattern measurements (Fig. S19). It can be seen that there is a significant difference between

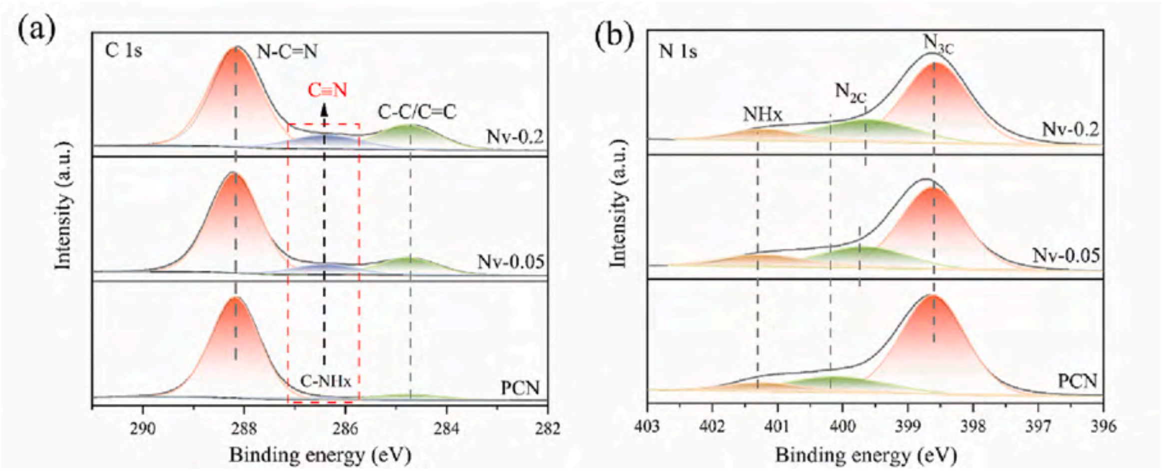

Fig. 4. (a) C 1 s XPS, (b) N 1 s XPS of PCN, Nv-0.05, and Nv-0.2.

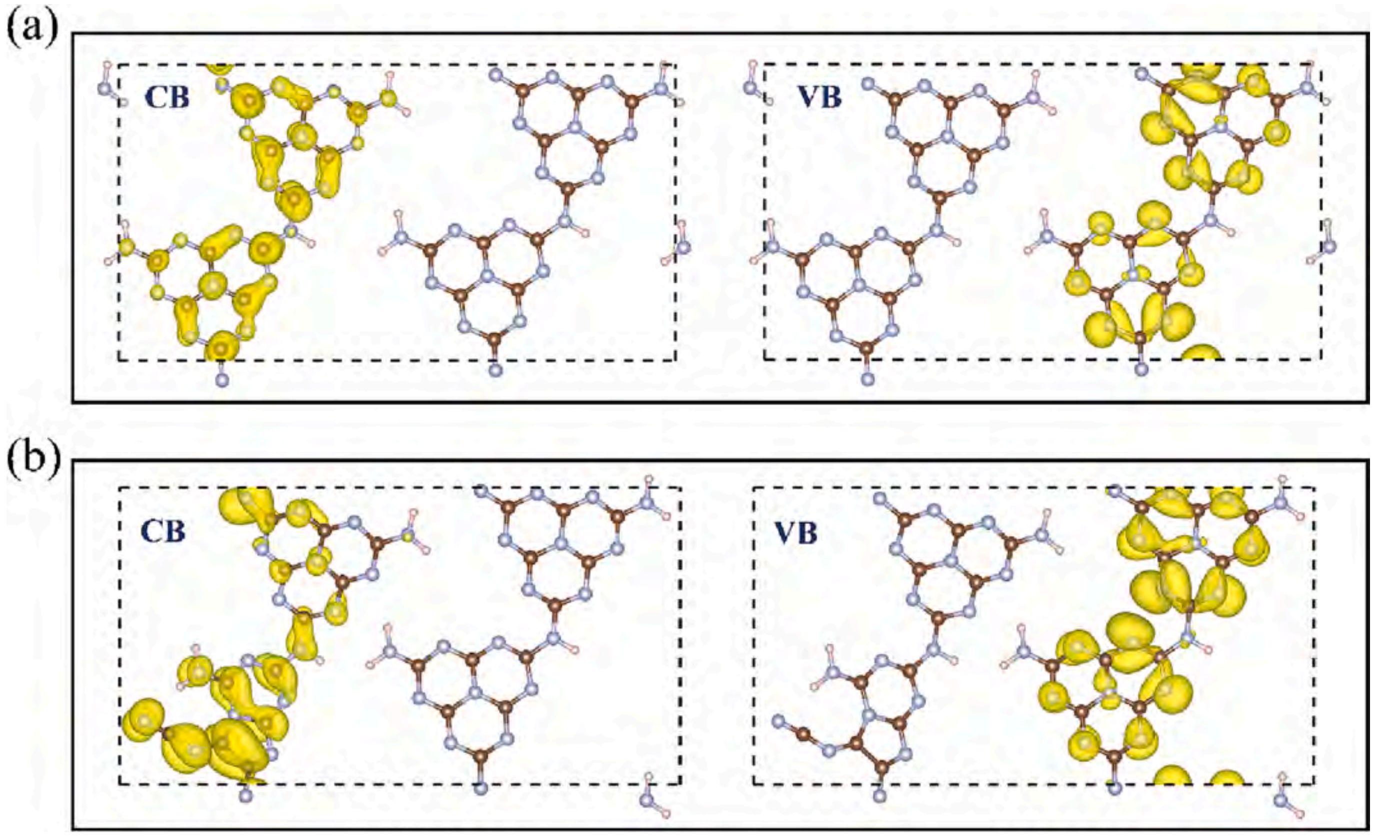

Fig. 5. (a) Calculated charge density distribution of CB and VB in PCN and (b) Nv-M. The isosurface value is 0.003 e Å $^{-3}$. The blue, brown, and pink spheres represent N, C, and H atoms, respectively.

the surface potentials of PCN and Nv-0.05. The distribution of the surface potential distribution was in the range of 210 ~ 240, and 550 ~ 590 mv, respectively. The IEF was calculated to obtain the IEF and found to be 5.43 times higher for Nv-0.05 than for PCN (Fig. S20).

After absorbing the photons, the photocatalysts in the excited state will jump to the ground state through the emission of fluorescence [59]. The photoluminescence (PL) spectra were used to analyze the physicochemical properties of systems indirectly [60]. As shown in Fig. 6a, a relatively strong fluorescence signal was recorded in PCN, while the emission intensity observed from Nv-M decreased obviously. The comparisons demonstrated that the huge PL decay in Nv-M was mainly caused by the suppression of electron and hole recombination, and also suggested that the IEF tuning by N defects was capable of boosting charge separation significantly. Furthermore, since the stronger photon absorption of Nv-M than PCN, the proportion of the non-emissive states excited states covered by charge trapping should be much larger than that of PCN [61]. To further illuminate the variation in charge-carrier dynamics induced by defect structure, the decay dynamics of the emissive states were subsequently investigated via time-resolved photoluminescence (TRPL) spectrum. Fig. 6b and Table S3 indicated that Nv-M shows a more rapid PL decay kinetic, where the average lifetime of PCN, Nv-0.05, and Nv-0.2 were 9.46, 7.18, and 5.49 ns, respectively. A short lifetime of Nv-M were attributed to the rapid capture of electrons by cyano group and N vacancy. This constantly accelerates the degradation of electronics lifetime and effectively suppresses carrier recombination [62,63]. The smaller radius of EIS Nyquist plots (Fig. 6c) and larger photocurrent (Fig. 6d) of Nv-0.05 compared to PCN. It substantiated that Nv-M has lower mass transfer impedance and better carrier transfer performance This change could be explained by the introduction of N vacancies and cyano groups that successfully built IEF to promote separation of photogenerated carriers [37,54].

3.4. Photocatalytic performance of H_2O_2 production and TC degradation

The photocatalytic activities of the catalysts for H_2O_2 production were evaluated in aqueous solution under visible light irradiation. First, the photocatalytic activity was tested for time-dependent light-driven H_2O_2 production of different samples in aqueous solution (10% IPA; pH = 7), as shown in Fig. 7a and Fig. S7a. It was discovered that Nv-M exhibited superior efficiency toward H_2O_2 production than PCN (approximately 7 times), with an H_2O_2 evolution rate of 623.5 μmol $g^{-1}h^{-1}$. The enhancement of photocatalytic H_2O_2 production was ascribed to the introduced of N vacancies and cyano groups in Nv-M framework, which successfully constructed IEF for promoting the separation of photogenerated charge vacancies. The trend of H_2O_2 produced by Nv-0.05 with time was shown in Fig. S7b, with a gradual increase in absorption value at 350 nm. The Nv-0.05 exhibited the best photocatalytic activity with a H_2O_2 production rate of 10.63×10^{-6} M min^{-1} (Fig. S7c) under visible-light irradiation. In contrast, Nv-0.2 exhibited lower H_2O_2 production activity, which is possibly related to the specific surface area decrease and the serious disruption of ordered structures within the framework of the KOH etching impact. It is found that the appropriate use of KOH not only successfully introduces N defects into Nv-M, but also ensures the properly specific surface to provide more reduction and oxidation sites, thus effectively suppressing carrier recombination. Besides, H_2O_2 can be decomposed as soon as it is produced by reacting with CB electrons and VB holes. ($H_2O_2 + H^+ + e^- = H_2O + \cdot OH$; $H_2O_2 + H^+ + 2e^- = H_2O$; $H_2O_2 + h^+ = H^+ + HO_2$; $H_2O_2 + 2h^+ = O_2 + 2H^+$). The photo-stationary concentration of H_2O_2 depends on the competition between the formation rate (k_f) and decomposition rate (k_d) of H_2O_2 over the catalysts, with the formula: $[H_2O_2] = (k_f \ / \ k_d)\{1 - \exp(-k_d \times t)$. [21] Fig. S8 showed that Nv-0.05 exhibited higher k_f and lower k_d than PCN. This may be attributed to the introduction of cyano groups in the modified material, replacing the amino group which is more attractive to H_2O_2

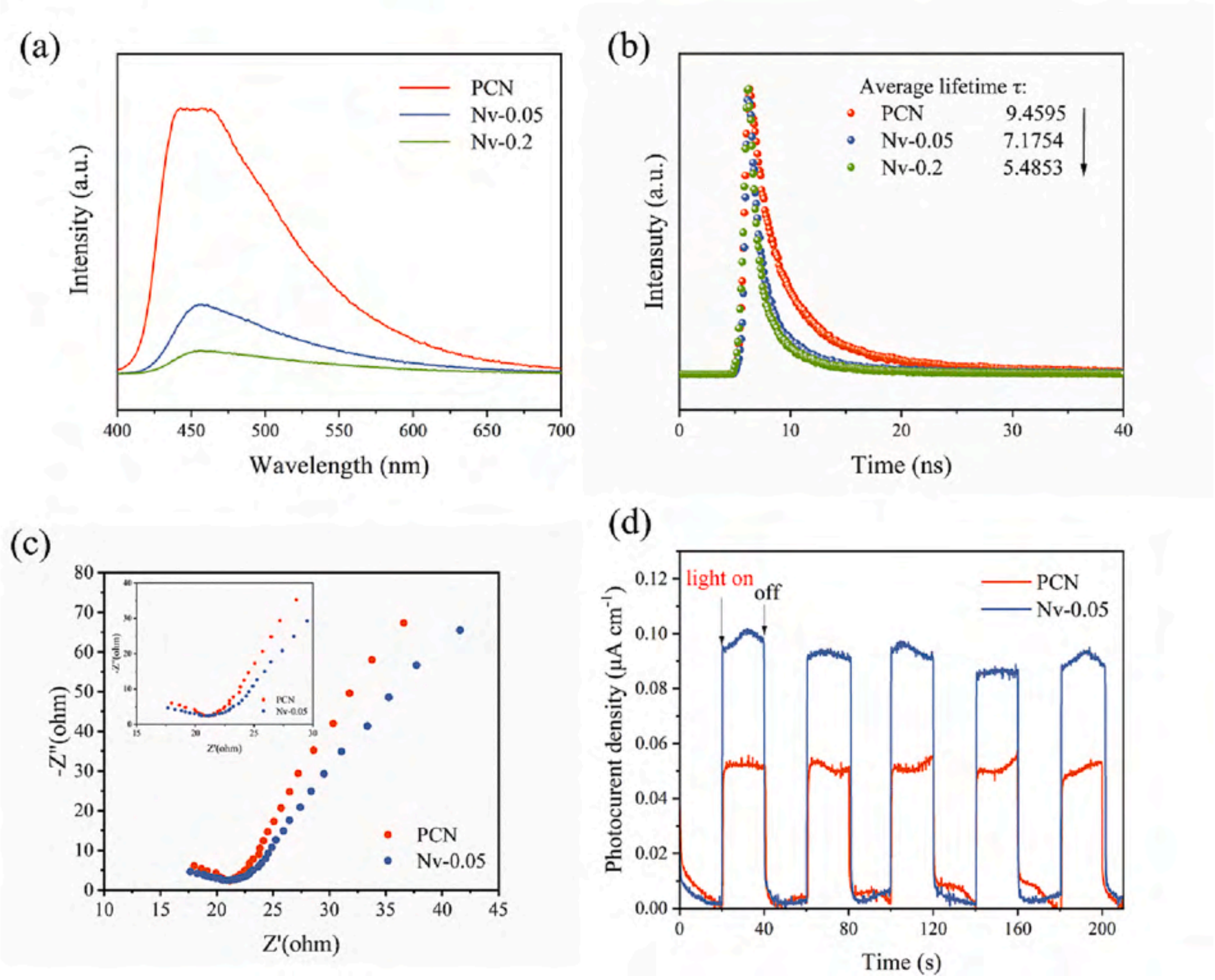

Fig. 6. (a) Photoluminescence (PL) spectra and (b) time-resolved photoluminescence (TRPL) of PCN, Nv-0.05, and Nv-0.2. (c) Electrochemical chemical impedance spectra (EIS) of PCN and Nv-0.05. (d) Transient photocurrent response curves of PCN and Nv-0.05 under visible light irradiation.

[22,64]. In addition, Nv-0.05 has a small specific surface area and relatively few active sites for H_2O_2 adsorption. The low adsorption capacity for H_2O_2 inhibits the reaction of in situ generated H_2O_2 with surface electrons and holes [65,66]. The adsorption experiments were further investigated (1 mM H_2O_2, stirring for 30 min in the dark). With $[H_2O_2]_{ad}$ = 98.57 μM for Nv-0.05 (surface area 62.22 m^2 g^{-1}) and $[H_2O_2]ad$ = 112.81 μM for PCN (surface area 86.42 m^2 g^{-1}). The results showed that Nv-0.05 has a lower adsorption capacity for H_2O_2. Combining with Fig. S8a, it can be seen that PCN shows H_2O_2 decomposition activity under visible light irradiation conditions. In contrast, Nv-0.05 hardly decomposes H_2O_2, which makes Nv-0.05 have higher H_2O_2 production efficiency. Indicating that N defects modification not only encouraged the generation of H_2O_2, but also inhibited the subsequent decomposition of H_2O_2 (Fig. S5).

Since the generation of H_2O_2 by proton-coupled electron transfer to dioxygen, the continuous supply of protons (H^+) during the reaction and the adsorption performance of the material on H^+ directly determined the H_2O_2 generation efficiency [9]. It has been demonstrated that the weak acidic conditions with high concentrations of protons contributed to the efficient production of H_2O_2 from Nv-0.05 (Figs. 7b and S9). When the pH value was further lowered from pH 5 to pH 3, the competition between the H_2 evolution ($2H^+ + 2e^- \rightarrow H_2$, $E = 0\ V_{NHE}$) and the H_2O_2 production would decrease the generation activity of H_2O_2 [59,67]. Furthermore, the production performance of H_2O_2 under visible light without adding IPA was also tested. As shown in Fig. S10, Nv-0.05 produced the highest amounts of H_2O_2. The efficiency of photocatalytic H_2O_2 production in pure water is relatively low. It was found that the H_2O_2 generation efficiency of Nv-0.05 in the IPA system was greatly improved compared to that of pure water (about 10 times). This was due to the fact that protons can react with surface O_2 rapidly by adding IPA as a sacrificial agent to donate protons. The improved Nv-M material has a stronger O_2 adsorption capacity and a higher carrier transport efficiency. Protons can swiftly react with surface O_2 by being added to IPA as a sacrificial agent to donate protons, which significantly enhancing the production efficiency of H_2O_2 [50]. As shown in Fig. 7d, the light utilization efficiency of Nv-0.05 was assessed by analyzing the apparent quantum yield (AQY) under monochromatic light irradiation. The above results showed that the trends of AQY and the absorption spectrum of the samples are almost consistent. Under visible light irradiation conditions, Nv-0.05 displayed a superior AQY, which reached 50.5% and 29.3% at 400 nm and 420 nm, respectively. At the same time, the solar to chemical energy conversion (SCC) efficiencies of the best performing Nv-0.05 were measured to be 0.27% (Fig. 7c) under AM 1.5G simulated sunlight (1 sun). According to the aforesaid finding, Nv-0.05 shows a high light utilization efficiency. Moreover, Figs. S11 and S12 showed that the photocatalytic activity of Nv-0.05 did not significantly decrease after continuous cycling (five times) photo generation H_2O_2 tests, indicating that Nv-0.05 has good cyclability and stability.

Using the antibiotic molecule TC as a model, the potential application of Nv-M in environmental remediation was further investigated [68]. As shown in Fig. 8a, the Nv-0.05 exhibited an efficient TC degradation (73.5%) under visible light irradiation over 40 min. However, the addition of excess KOH during the synthesis would decrease the photocatalytic degradation activity of TC, which corresponds to the same

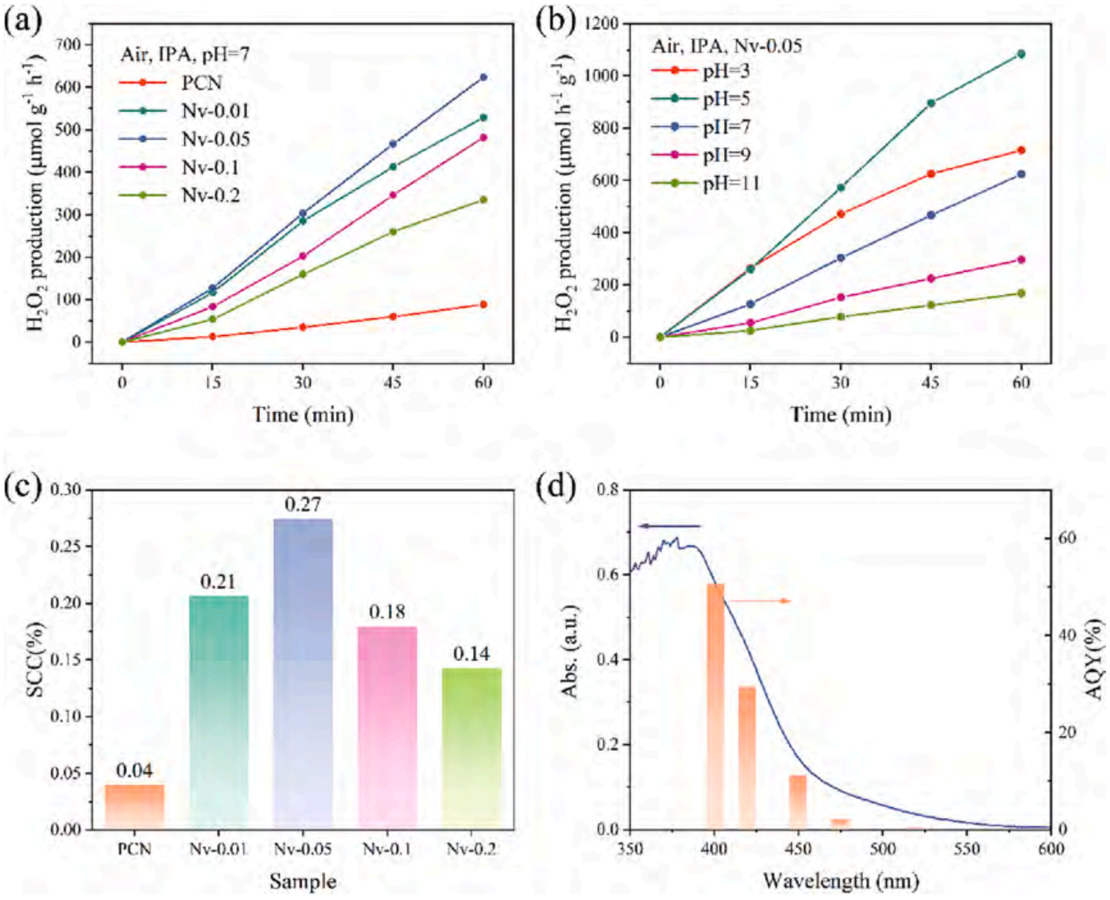

Fig. 7. (a) Time course of H_2O_2 generation test under visible light irradiation. ($\lambda \geq 420$ nm, 40 mW cm^{-2}; 1 g L^{-1} catalyst). (b) The pH-dependent generation of H_2O_2 on Nv-0.05 under visible-light-irradiation. (c) Efficiency of SCC for H_2O_2 production. (d) AQY of H_2O_2 production as a function of the irradiation wavelength (10% IPA; 1 g L^{-1} catalyst; pH = 7).

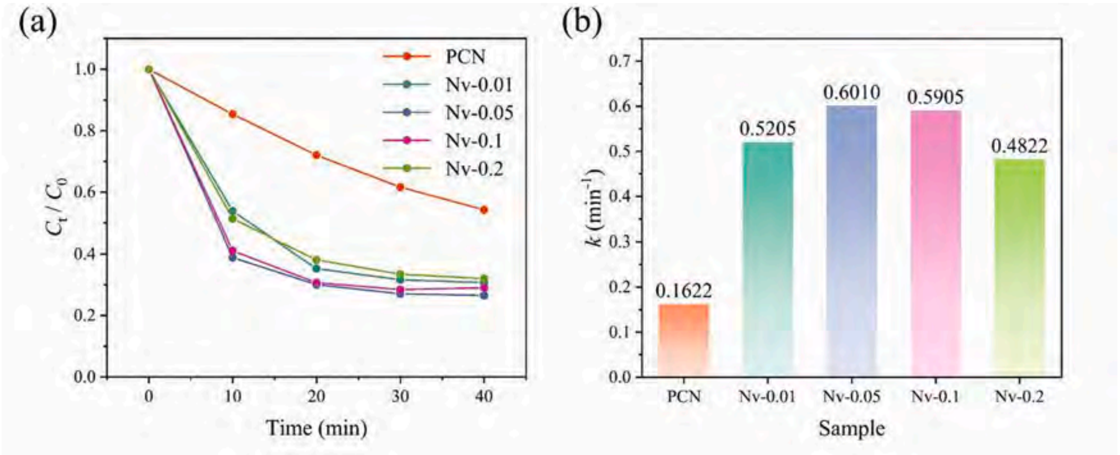

Fig. 8. (a) Photodegradation efficiency of TC under visible light irradiation for different times on all samples. (b) The corresponding reaction dynamic data.

trend as the photocatalytic generation H_2O_2. This phenomenon further confirmed that an excess of KOH would damage the ordered structures within the framework. The decreased specific surface area would influence the active sites on the catalyst surface and thus photocatalytic activity [69]. The kinetic rates of degradation TC for Nv-0.05 was 6.010 min^{-1}, which was almost 3.7 times that of PCN (Fig. 8b). Meanwhile, Nv–0.05 degraded TC with good cyclability (Figs. S12 and 13). It can be seen that modified g-C_3N_4 by defect showed superb photocatalytic activity for pollutant degradation and certain perspectives of application in the environmental remediation. Based on the above results, the composite system of both H_2O_2 generation and TC degradation with Nv-M has been investigated here. As shown in Fig. 9c, the yield of H_2O_2 improved from 623.5 to 695.6 μmol g^{-1} h^{-1}, while the TC degradation efficiency was slightly reduced from 73.5% to 69.5%. The composite system promoted the generation of H_2O_2 and slightly inhibits the degradation of TC. The phenomenon may be due to the competition between the two systems for the free radicals who play a major role in the reaction, which has been confirmed in the following mechanistic

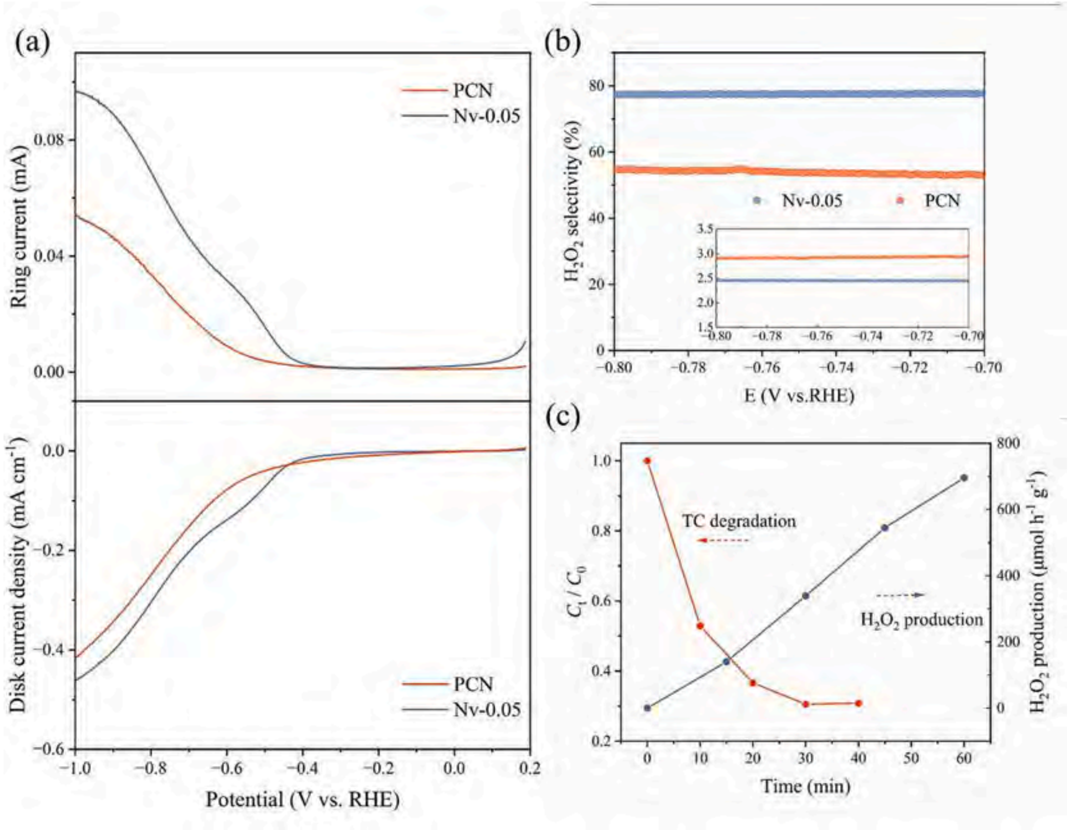

Fig. 9. (a) RRDE polarization curves over PCN- and Nv-0.05-coated electrodes at 1600 rpm in O_2-saturated electrolyte using the ring current (top) and the disc current (bottom). (b) H_2O_2 selectivity as a function of the applied potential. The corresponding average number of transferred electrons (n) is shown in the inset. (c) The composite system of H_2O_2 generation and TC degradation.

studies. On the other hand, the H_2O_2 generation and TC degradation in the composite system was just slightly influenced, which means that Nv-M application in the composite system was feasible.

3.5. Experimental mechanism of photocatalytic H_2O_2 evolution

The $2e^-$ ORR pathway is of serious importance for H_2O_2 generation [39]. The effect of N defects in Nv-M on O_2 selective electron transfer was investigated via analysis of the rotating ring-disc electrode (RRDE). The reduction process of oxygen generated a disc current ($O_2 + 2e^- + 2H^+ \rightarrow H_2O_2$ or $O_2 + 4e^- + 4H^+ \rightarrow H_2O$) while the oxidation process of H_2O_2 generated a ring current ($H_2O_2 \rightarrow O_2 + 2H^+ + 2e^-$) [70]. In Fig. 9a, the monitored selectivity for H_2O_2 production in an O_2-saturated 0.1 M H_3PO_4 electrolyte was compared with PCN and Nv–0.05. Notably, the Nv-0.05 disc current was enhanced with the decreasing potential below −0.4 V (vs. RHE), just like that of PCN (Fig. 9, bottom). Since the H_2O_2 generated on the disk part was able to be rapidly transported to the ring part, the positive oxidation current on the ring electrode was measured (Fig. 9a, top). Nv-0.05 exhibited relatively higher ring current than PCN, indicating that a higher H_2O_2 yields when the potential was in the range of −0.80 to −0.70 V with a corresponding selectivity of 78 % (Fig. 9b). While PCN exhibited 52% H_2O_2 selectivity under the same test condition, further confirming the importance of N defects in encouraging the catalytic activity. The calculated average number of transferred electrons (Fig. 9b) for PCN and Nv-0.05 were 2.92 and 2.45 (at −0.75 V vs. RHE), respectively, suggesting that Nv-0.05 is more selective for the $2e^-$ ORR [61,71]. The RRDE measurements are consistent with the ability of photocatalytic-producting H_2O_2. All above measurements demonstrated that Nv-0.05 exhibited higher $2e^-$ ORR activity and selectivity, which was attributed to the N defects modification that are particularly beneficial to the $2e^-$ ORR pathway.

To unravel the reactive species responsible for photocatalytic H_2O_2 production, $AgNO_3$, EDTA-2Na, TEMPOL, L-tryptophan and methanol were used as e^-, h^+, $\cdot O_2^-$, $^1O_2$, •OH scavengers, respectively [51]. In Fig. 10a, the production of H_2O_2 dropped sharply while $AgNO_3$ was used as a scavenger, demonstrating that electrons play an essential part during the H_2O_2 generation process. However, the equilibrium concentration of H_2O_2 was mildly raised when used EDTA-2Na as a scavenger, which was ascribe to the enhanced electron utilization by the holes trapping. After the addition of TEMPOL and L-tryptophan, respectively, the yield of H_2O_2 was almost inhibited, indicating that the $\cdot O_2^-$ and $^1O_2$ were essential species during the process of photosynthetic H_2O_2. On the contrary, the addition of methanol has insignificant effect on the generation of H_2O_2, which means that •OH had no contribution to the photocatalytic production of H_2O_2. In addition, the generation of $\cdot O_2^-$ and $^1O_2$ in photocatalytic reactions was examined by using EPR. In Fig. 10c and Fig. 10d, the DMPO-$\cdot O_2^-$ signals and the TEMP-$^1O_2$ signals are noticed after light illumination, indicating that both $\cdot O_2^-$ and $^1O_2$ are the main ROS in the photocatalytic reaction. According to the results, the photo-excited catalyst produced $\cdot O_2$ and $^1O_2$ on the surface, and both of them effectively reacted with the electrons to produce H_2O_2 and degrade TC. Therefore, the two kinds of reaction would struggle with one another for the free radical in the composite system, which seems to encourage the generation of H_2O_2 and mildly inhibit the degradation of TC. Based on the previous reports [72,73], it is suggested that Nv-0.05 reduced oxygen molecules to produce H_2O_2 through a two-electron reaction ($O_2 \rightarrow \cdot O_2^- \rightarrow H_2O_2$) and released oxygen by oxidizing water through a four-electron reaction ($H_2O \rightarrow O_2$).

Subsequently, it was observed that the photocatalytic H_2O_2 yield decreased sharply after the reaction solution was bubbled with N_2 for 60 min (Fig. 10a and Fig. S14), suggesting that O_2 was an essential reactant in the catalytic reaction. In addition, there was no discernible difference

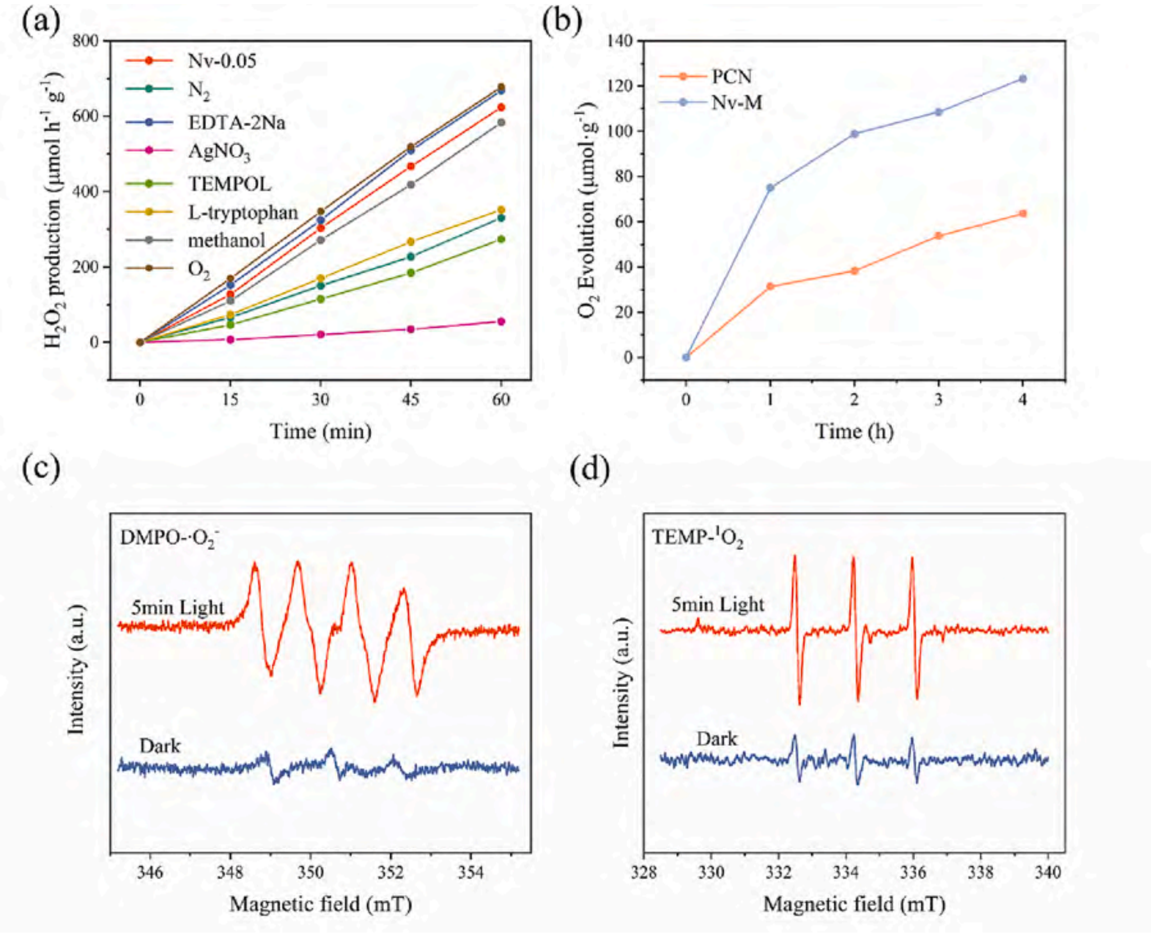

Fig. 10. (a) H_2O_2 generation curves over Nv-0.05 alone and with different quenchers under visible light illumination. (b) The photocatalytic O_2 production activities of the PCN and Nv-0.05. (c, d) ESR signals for DMPO-•O_2^- and DMPO-$^1O_2$ over Nv-0.05 sample.

in H_2O_2 generation under air and O_2 bubbling conditions. This indicated that the modified catalysis has exceptional O_2 adsorption capability and the Nv-M can still effectively generate H_2O_2 under air conditions. The precondition for the formation of OOH* was the adsorption of O_2 and H^+ on catalyst surfaces, and then the formation of OOH* and subsequent hydrogenation is the key to the 2e$^-$ ORR activity toward H_2O_2 [39,74,75]. An exothermic process with a large negative adsorption energy of O_2 is estimated with PCN and the optimal structure of at the cyano and N vacancy site of Nv-M. In Fig. 11 and Fig. S15, the O_2 adsorption energy at N vacancy (−0.22 eV) on Nv-M was obviously smaller than the cyano group sites (−0.15 eV) and PCN (0.76 eV). Fig. S23 showed the programmed temperature desorption O_2 (TPD-O_2) curves of PCN and Nv-0.05. It was obviously that the Nv-0.05 has stronger adsorption capacity and surface bonding strength of O_2. This results was consistent with the theoretical calculations. The strong O_2 adsorption property of Nv-0.05 efficiency promoted the generation of H_2O_2 via 2e$^-$ ORR. It is demonstrated that N vacancies have a preference for attracting O_2, while cyano has significant electron-withdrawing

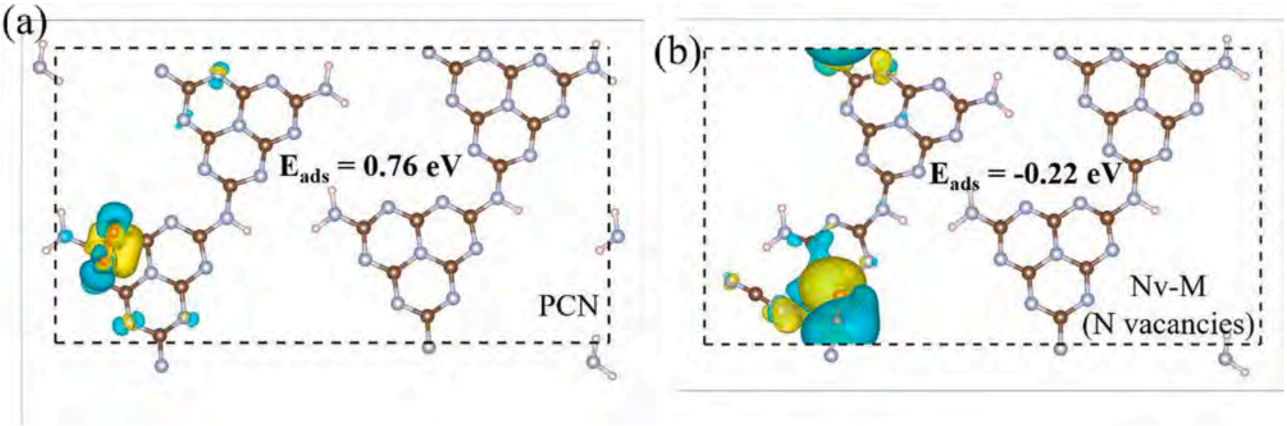

Fig. 11. Top views of the structure with different charge densities for O_2 adsorption on PCN (a) and Nv-M (b). Green and blue isosurfaces represent electron and hole distributions, respectively. The isosurface value is 0.008 e Å^{-3}. The blue, brown, pink, and red spheres represent N, C, H, and O atoms, respectively.

properties (shown in previous studies) [37,39], facilitating the interaction of adsorbed $*O_2$ with H^+ and e^-. The addition of N defects to Nv-M may improve how well adsorbed $*O_2$ and H^+ interact with e^-. This promoted the $2e^-$ ORR pathway even more, which in turn encourages the production of H_2O_2. Furthermore, the photocatalytic O_2 generation activities of the PCN and Nv-0.05 were compared in order to clarify the function of photogenerated holes in the reaction system. In Fig. 10b, the photocatalytic O_2 yield of Nv-0.05 was almost twice as high as that of PCN under the same conditions. This suggested that the water oxidation behavior of releasing oxygen via a four-electron reaction, as well as the effective suppression of electron-hole recombination (combined with Fig. 6a–d). According to the above tests and experiments, the electrons were involved in the oxygen reduction reaction to generated H_2O_2, and the holes were involved in the water oxidation reaction to release O_2.

To further reveal the photocatalytic degradation mechanism of Nv-0.05 and the contribution of radical species during TC photodegradation, different charge scavengers were introduced to identify the specific radicals in the photodegradation reaction. As shown in Fig. S16, the photocatalytic performance of Nv-0.05 was dropped slightly after adding TEMPOL and L-tryptophan to the photoreaction system, respectively. The result indicated that $\cdot O_2^-$ and $^1O_2$ played the significant role as oxidative species in the photodegradation process. According to the quenching experiment, it was obvious that the $\cdot OH$ and H_2O_2 did not play the role of oxidative degradation of TC in the system. Moreover, the ESR (Fig. 10c and Fig. 10d) confirm that two kinds of free radicals were activated during the photodegradation process. In addition, incorporating N vacancies and cyano groups into Nv-M can further modulate the charge-density distribution and construct IEF, suppressing the recombination of photogenerated electron-holes. As a result, the electrons can be transported quickly and react with activated ROS ($\cdot O_2$, $^1O_2$), which is the key to improving the photocatalytic activity.

As shown in Fig. 12, according to the results of above analysis, the Nv-0.05 photocatalytic production mechanism of H_2O_2 in the presence of IPA and TC degradation mechanism were proposed. Under visible light irradiation, the electrons and holes created by Nv–M absorbing photons were transported to the active site rapidly. The trapped holes quickly react with IPA to release protons, which then attached to the catalytic surface. Photo-generated holes oxidize IPA and produce hydrogen ions and acetone [52]. The CB position of Nv-0.05 (-0.43 V vs. NHE, Fig. S3) was below the standard reduction potential of $O_2/\cdot O_2^-$ (–0.33 V vs. NHE) [76]. This may facilitate the reaction of electrons from CB with the adsorbed O_2 to form $\cdot O_2^-$ [77]. Moreover, the generated $^1O_2$ may be converted from $\cdot O_2^-$, the free ROS can immediately react with H^+ to generate H_2O_2 [52]. And the CB potential still has enough energy to drive the $2e^-$ reduction of O_2 to H_2O_2 (0.69 V vs. NHE). Moreover, with the creation of the N defects, the Nv-0.05 exhibited enhanced O_2 adsorption and high $2e^-$ ORR selectivity, dramatically accelerating the H_2O_2 production efficiency (1)(2)(3)(4)(5)(6)(7)(8). The efficient separation of photogenerated electron-holes can oxidize H_2O to release O_2 (8). For the degradation of TC, the photogenerated electrons and holes were formed on Nv-0.05 under the visible light irradiation. Then create ROS ($\cdot O_2^-$, $^1O_2$). Later on, under the attack of $\cdot O_2^-$ and $^1O_2$, the organic molecule TC was decomposed into non-toxic molecules or mineralized. (1), (4), (5), (7), (10) [9,77,78].

$$Nv-M + hv \rightarrow e^- + h^+ \tag{1}$$

$$(CH_3)_2CH_2OH + 2h^+ \rightarrow (CH_3)_2CO\cdot + 2H^+ \tag{2}$$

$$O_2 + 2H^+ + 2e^- \rightarrow H_2O_2 \tag{3}$$

$$O_2 + e^- \rightarrow \cdot O_{2^-} \tag{4}$$

$$\cdot O_{2^-} + h + \rightarrow \ ^1O_2 \tag{5}$$

$$\cdot O_{2^-} + e^- + 2H^+ \rightarrow H_2O_2 \tag{6}$$

$$O_2 \rightarrow \ ^1O_2 \tag{7}$$

$$^1O_2 + 2H^+ + 2e^- \rightarrow H_2O_2 \tag{8}$$

$$2H_2O + 4h^+ \rightarrow O_2 + 4H^+ \tag{9}$$

$$(\cdot O_{2^-}, \ ^1O_2) + TC \rightarrow CO_2 + H_2O \tag{10}$$

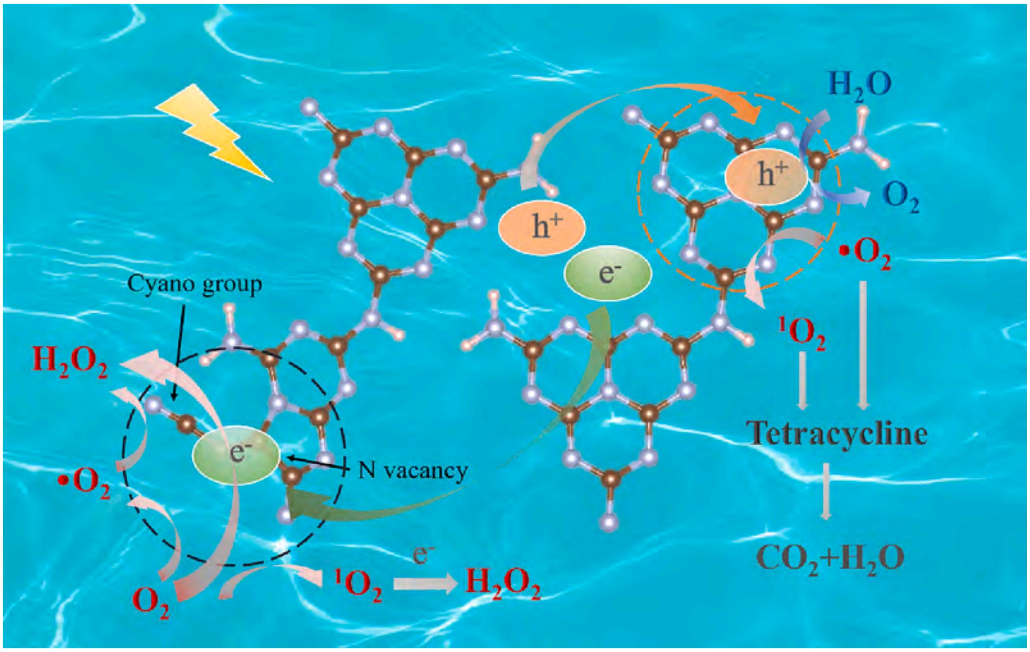

Fig. 12. Schematic diagram of the N vacancies and cyano group modification in Nv-M synergistically promoting the photocatalytic H_2O_2 generation and TC degradation. The blue, brown, red spheres represent N, C, and H atoms, respectively.

4. Conclusion

In summary, using the IPA as the electron/proton donor during the visible-light-driven selective 2e$^-$ ORR, the carbon nitride framework with N vacancies and cyano group exhibits excellent photocatalytic activity for H_2O_2 generation. The production of H_2O_2 by Nv-0.05 reached 623.5 μM within 1 h, almost 7 times higher than that of the PCN. In addition, the Nv-0.05 exhibits a superior performance for degradation TC. The introduction of the N vacancies and cyano group into the Nv-M framework has the following multiple influence: (1) enhance the visible light absorption and change the energy band structure of the photocatalysts, (2) improve the transport of carriers and successfully establish an internal electric field, further effectively suppressing carrier recombination, (3) construct surface active sites for dioxygen adsorption to promote the generation of $^{\bullet}O_2^-$ and $^1O_2$, and (4) facilitate selective 2e$^-$ ORR and oxidize water to produce O_2, all of which have a property of synergistically promoting visible-light-driven H_2O_2 generation and TC degradation. It is particularly worth-noting that H_2O_2 can be generated through a variety of pathways, proving the main roles of $^1O_2$ that was overlooked in previous studies, and suggesting an effective way to further increase the production of H_2O_2.

Declaration of Competing Interest

The authors declare that they have no known competing financial interests or personal relationships that could have appeared to influence the work reported in this paper.

Data availability

Data will be made available on request.

Acknowledgements

This study was supported by the Innovative Province Construction Special Fund of Hunan province (2020SK2016) and the Water Conservancy Science and Technology Project of Hunan Province (XSKJ2021000-47).

Appendix A. Supplementary data

Supplementary data to this article can be found online at https://doi.org/10.1016/j.cej.2023.142512.

References

[1] S.C. Perry, D. Pangotra, L. Vieira, L.I. Csepei, V. Sieber, L. Wang, C.P. de Leon, F. C. Walsh, Electrochemical synthesis of hydrogen peroxide from water and oxygen, Nat. Rev. Chem. 3 (7) (2019) 442–458.

[2] L.F.D.E. Freitas, B. Puertolas, J. Zhang, B.W. Wang, A.S. Hoffman, S.R. Bare, J. Perez-Ramirez, J.W. Medlin, E. Nikolla, Tunable catalytic performance of palladium nanoparticles for H2O2 direct synthesis via surface-bound ligands, ACS Catal. 10 (9) (2020) 5202–5207.

[3] J.K. An, N. Li, Q. Zhao, Y.J. Qiao, S. Wang, C.M. Liao, L. Zhou, T. Li, X. Wang, Y. J. Feng, Highly efficient electro-generation of H2O2 by adjusting liquid-gas solid three phase interfaces of porous carbonaceous cathode during oxygen reduction reaction, Water Res. 164 (2019).

[4] Z. Wei, M.L. Liu, Z.J. Zhang, W.Q. Yao, H.W. Tan, Y.F. Zhu, Efficient visible-light-driven selective oxygen reduction to hydrogen peroxide by oxygen-enriched graphitic carbon nitride polymers, Energy Environ. Sci. 11 (9) (2018) 2581–2589.

[5] J.J. Hu, S. Wang, J.Q. Yu, W.K. Nie, J. Sun, S.B. Wang, Duet Fe3C and FeNx Sites for H2O2 generation and activation toward enhanced electro-fenton performance in wastewater treatment, Environ. Sci. Tech. 55 (2) (2021) 1260–1269.

[6] R.J. Watts, A.L. Teel, Hydroxyl radical and non-hydroxyl radical pathways for trichloroethylene and perchloroethylene degradation in catalyzed H2O2 propagation systems, Water Res. 159 (2019) 46–54.

[7] J. Xiao, Q. Liu, M.A. Song, X.R. Li, Q. Li, J.K. Shang, Directing photocatalytic pathway to exceedingly high antibacterial activity in water by functionalizing holey ultrathin nanosheets of graphitic carbon nitride, Water Res. 198 (2021).

[8] C.Y. Zhang, H. Wang, H.B. Yu, K.X. Yi, W. Zhang, X.Z. Yuan, J.H. Huang, Y. C. Deng, G.M. Zeng, Single-atom catalysts for hydrogen generation: rational design, recent advances, and perspectives, Adv. Energy Mater. 12 (27) (2022).

[9] J.S. Cai, J.Y. Huang, S.C. Wang, J. Iocozzia, Z.T. Sun, J.Y. Sun, Y.K. Yang, Y.K. Lai, Z.Q. Lin, Crafting mussel-inspired metal nanoparticle-decorated ultrathin graphitic carbon nitride for the degradation of chemical pollutants and production of chemical resources, Adv. Mater. 31 (15) (2019).

[10] J.M. Campos-Martin, G. Blanco-Brieva, J.L.G. Fierro, Hydrogen peroxide synthesis: An outlook beyond the anthraquinone process, Angew. Chem. Int. Ed. 45 (42) (2006) 6962–6984.

[11] S. Liu, J.H. Huang, W. Zhang, L.X. Shi, K.X. Yi, C.Y. Zhang, H.L. Pang, J.N. Li, S. Z. Li, Investigation of the adsorption behavior of Pb(II) onto natural-aged microplastics as affected by salt ions, J. Hazard. Mater. 431 (2022).

[12] Y. Shiraishi, T. Takii, T. Hagi, S. Mori, Y. Kofuji, Y. Kitagawa, S. Tanaka, S. Ichikawa, T. Hirai, Resorcinol-formaldehyde resins as metal-free semiconductor photocatalysts for solar-to-hydrogen peroxide energy conversion, Nat. Mater. 18 (9) (2019) 985.

[13] R.F. Du, K. Xiao, B.Y. Li, X. Han, C.Q. Zhang, X. Wang, Y. Zuo, P. Guardia, J.S. Li, J. B. Chen, J. Arbiol, A. Cabot, Controlled oxygen doping in highly dispersed Ni-loaded g-C3N4 nanotubes for efficient photocatalytic H2O2 production, Chem. Eng. J. 441 (2022).

[14] J.H. Huang, Y.L. Gu, G.M. Zeng, Y. Yang, Y.C. Ouyang, L.X. Shi, Y.H. Shi, K.X. Yi, Control of indigenous quorum quenching bacteria on membrane biofouling in a short-period MBR, Bioresour. Technol. 283 (2019) 261–269.

[15] L. Shi, J. Huang, L. Zhu, Y. Shi, K. Yi, X. Li, Role of concentration polarization in cross flow micellar enhanced ultrafiltration of cadmium with low surfactant concentration, Chemosphere 237 (2019), 124859.

[16] K. Mase, M. Yoneda, Y. Yamada, S. Fukuzumi, Seawater usable for production and consumption of hydrogen peroxide as a solar fuel, Nat. Commun. 7 (2016).

[17] H.N. Che, X. Gao, J. Chen, J. Hou, Y.H. Ao, P.F. Wang, Iodide-induced fragmentation of polymerized hydrophilic carbon nitride for high-performance quasi-homogeneous photocatalytic H2O2 production, Angew. Chem. Int. Ed. 60 (48) (2021) 25546–25550.

[18] C. Chen, M. Yasugi, L. Yu, Z.Y. Teng, T. Ohno, Visible light-driven H2O2 synthesis by a Cu3BiS3 photocathode via a photoelectrochemical indirect two-electron oxygen reduction reaction, Appl. Catal. B Environ. 307 (2022).

[19] L. Yang, G. Dong, D.L. Jacobs, Y. Wang, L. Zang, C. Wang, Two-channel photocatalytic production of H2O2 over g-C3N4 nanosheets modified with perylene imides, J. Catal. 352 (2017) 274–281.

[20] S. Li, G. Dong, R. Hailili, L. Yang, Y. Li, F. Wang, Y. Zeng, C. Wang, Effective photocatalytic H2O2 production under visible light irradiation at g-C3N4 modulated by carbon vacancies, Appl. Catal. B 190 (2016) 26–35.

[21] H.-I. Kim, O.S. Kwon, S. Kim, W. Choi, J.-H. Kim, Harnessing low energy photons (635 nm) for the production of H2O2 using upconversion nanohybrid photocatalysts, Energy Environ. Sci. 9 (3) (2016) 1063–1073.

[22] Y. Shiraishi, Y. Kofuji, H. Sakamoto, S. Tanaka, S. Ichikawa, T. Hirai, Effects of surface defects on photocatalytic H2O2 production by mesoporous graphitic carbon nitride under visible light irradiation, ACS Catal. 5 (5) (2015) 3058–3066.

[23] G. Liu, Z. Tang, X. Gu, N. Li, H. Lv, Y. Huang, Y. Zeng, M. Yuan, Q. Meng, Y. Zhou, C. Wang, Boosting photocatalytic nitrogen reduction to ammonia by dual defective -C N and K-doping sites on graphitic carbon nitride nanorod arrays, Appl. Catal. B 317 (2022).

[24] A. Kumar, P. Raizada, A. Hosseini-Bandegharaei, V.K. Thakur, V. Nguyen, P. Singh, C-, N-Vacancy defect engineered polymeric carbon nitride towards photocatalysis: viewpoints and challenges, J. Mater. Chem. A 9 (1) (2021) 111–153.

[25] F. Li, X.Y. Yue, D.N. Zhang, J.J. Fan, Q.J. Xiang, Targeted regulation of exciton dissociation in graphitic carbon nitride by vacancy modification for efficient photocatalytic CO2 reduction, Appl. Catal. B-Environ. 292 (2021).

[26] S.S. Lam, V.H. Nguyen, M.T.N. Dinh, D.Q. Khieu, D.D. La, H.T. Nguyen, D.V.N. Vo, C.L. Xia, R.S. Varma, M. Shokouhimehr, C.C. Nguyen, Q.V. Le, W.X. Peng, Mainstream avenues for boosting graphitic carbon nitride efficiency: towards enhanced solar light-driven photocatalytic hydrogen production and environmental remediation, J. Mater. Chem. A 8 (21) (2020) 10571–10603.

[27] M. Majdoub, Z. Anfar, A. Amedlous, Emerging chemical functionalization of g-c3n4: covalent/noncovalent modifications and applications, ACS Nano 14 (10) (2020) 12390–12469.

[28] J. Huang, L. Zhu, G. Zeng, L. Shi, Y. Shi, K. Yi, X. Li, Recovery of Cd(II) and surfactant in permeate from MEUF by foam fractionation with anionic-nonionic surfactant mixtures, Colloids Surf. A Physicochem. Eng. Asp 570 (2019) 81–88, https://doi.org/10.1016/j.colsurfa.2019.03.010.

[29] V.W.H. Lau, I. Moudrakovski, T. Botari, S. Weinberger, M.B. Mesch, V. Duppel, J. Senker, V. Blum, B.V. Lotsch, Rational design of carbon nitride photocatalysts by identification of cyanamide defects as catalytically relevant sites, Nat. Commun. 7 (2016).

[30] Y. Ouyang, Y. Hu, J. Huang, Y. Gu, Y. Shi, K. Yi, Y. Yang, Effects of exogenous quorum quenching on microbial community dynamics and biofouling propensity of activated sludge in MBRs, Biochem. Eng. J. 157 (2020).

[31] X. Zhang, F. Tian, X. Lan, Y. Liu, W. Yang, J. Zhang, Y. Yu, Building P-doped MoS2/g-C3N4 layered heterojunction with a dual-internal electric field for efficient photocatalytic sterilization, Chem. Eng. J. 429 (2022).

[32] Y. Zeng, Q. Yin, Z. Liu, H. Dong, Attapulgite-interpenetrated g-C3N4/Bi2WO6 quantum-dots Z-scheme heterojunction for 2-mercaptobenzothiazole degradation with mechanism insight, Chem. Eng. J. 435 (2022).

[33] Q.Q. Fan, C.G. Niu, H. Guo, D.W. Huang, Z.T. Dong, Y.Y. Yang, H.Y. Liu, L. Li, M. Z. Qin, Insights into the role of reactive oxygen species in photocatalytic H(2)O(2) generation and OTC removal over a novel BN/Zn(3)In(2)S(6) heterojunction, J. Hazard. Mater. 438 (2022), 129483.

[34] J. Luo, C. Fan, L. Tang, Y. Liu, Z. Gong, T. Wu, X. Zhen, C. Feng, H. Feng, L. Wang, L. Xu, M. Yan, Reveal Brønsted–Evans–Polanyi relation and attack mechanisms of

reactive oxygen species for photocatalytic H2O2 production, Appl. Catal. B 301 (2022).

[35] H.L. Pang, K.X. Tian, Y.P. Li, C.L. Su, F. Duan, Y. Xu, Super-hydrophobic PTFE hollow fiber membrane fabricated by electrospinning of Pullulan/PTFE emulsion for membrane deamination, Sep. Purif. Technol. 274 (2021).

[36] L. Shi, Y. Lei, J. Huang, Y. Shi, K. Yi, H. Zhou, Ultrafiltration of oil-in-water emulsions using ceramic membrane: roles played by stabilized surfactants, Colloids Surf. A. Physicochem Eng. Asp 583 (2019).

[37] H.J. Yu, R. Shi, Y.X. Zhao, T. Bian, Y.F. Zhao, C. Zhou, G.I.N. Waterhouse, L.Z. Wu, C.H. Tung, T.R. Zhang, Alkali-assisted synthesis of nitrogen deficient graphitic carbon nitride with tunable band structures for efficient visible-light-driven hydrogen evolution, Adv. Mater. 29 (16) (2017).

[38] H.B. Yu, J.H. Huang, L.B. Jiang, L.J. Leng, K.X. Yi, W. Zhang, C.Y. Zhang, X. Z. Yuan, In situ construction of Sn-doped structurally compatible heterojunction with enhanced interfacial electric field for photocatalytic pollutants removal and CO2 reduction, Appl. Catal. B-Environ. 298 (2021).

[39] X. Zhang, P.J. Ma, C. Wang, L.Y. Gan, X.J. Chen, P. Zhang, Y. Wang, H. Li, L. H. Wang, X.Y. Zhou, K. Zheng, Unraveling the dual defect sites in graphite carbon nitride for ultra-high photocatalytic H2O2 evolution, Energy Environ. Sci. 15 (2) (2022) 830–842.

[40] Y.Y. Duan, Y. Wang, L.Y. Gan, J.Z. Meng, Y.J. Feng, K.W. Wang, K. Zhou, C. Wang, X.D. Han, X.Y. Zhou, Amorphous carbon nitride with three coordinate nitrogen (n3 (c)) vacancies for exceptional nox abatement in visible light, Adv. Energy Mater. 11 (19) (2021).

[41] J. Luo, C.Z. Fan, L. Tang, Y.N. Liu, Z.X. Gong, T.S. Wu, X.L. Zhen, C.Y. Feng, H. P. Feng, L.L. Wang, L. Xu, M. Yan, Reveal bronsted-evans-polanyi relation and attack mechanisms of reactive oxygen species for photocatalytic H2O2 production, Appl. Catal. B Environ. 301 (2022).

[42] J.H. Huang, J.L. Hu, Y.H. Shi, G.M. Zeng, W.J. Cheng, H.B. Yu, Y.L. Gu, L.X. Shi, K. X. Yi, Evaluation of self-cleaning and photocatalytic properties of modified g-C3N4 based PVDF membranes driven by visible light, J. Colloid. Interf. Sci. 541 (2019) 356–366.

[43] Y. Wang, P.P. Du, H.Z. Pan, L. Fu, Y. Zhang, J. Chen, Y.W. Du, N.J. Tang, G. Liu, Increasing solar absorption of atomically thin 2d carbon nitride sheets for enhanced visible-light photocatalysis, Adv. Mater. 31 (40) (2019).

[44] W.K. Wang, H.M. Zhang, S.B. Zhang, Y.Y. Liu, G.Z. Wang, C.H. Sun, H.J. Zhao, Potassium ion assisted regeneration of active cyano groups in carbon nitride nanoribbons: visible light driven photocatalytic nitrogen reduction, Angew. Chem. Int. Ed. 58 (46) (2019) 16644–16650.

[45] C. Yang, B. Wang, L.Z. Zhang, L. Yin, X.C. Wang, Synthesis of layered carbonitrides from biotic molecules for photoredox transformations, Angew. Chem. Int. Ed. 56 (23) (2017) 6627–6631.

[46] W. Li, Z. Wei, K. Zhu, W. Wei, J. Yang, J. Jing, D.L. Phillips, Y. Zhu, Nitrogen-defect induced trap states steering electron-hole migration in graphite carbon nitride, Appl. Catal. B 306 (2022).

[47] Z. Hong, B. Shen, Y. Chen, B. Lin, B. Gao, Enhancement of photocatalytic H2 evolution over nitrogen-deficient graphitic carbon nitride, J. Mater. Chem. A 1 (38) (2013).

[48] X. An, Q. Tang, H. Lan, H. Liu, X. Yu, J. Qu, H. Lin, J. Ye, Facilitating molecular activation and proton feeding by dual active sites on polymeric carbon nitride for efficient co(2) photoreduction, Angew. Chem. Int. Ed. Engl. 61 (46) (2022) e202212706.

[49] D.M. Zhao, C.L. Dong, B. Wang, C. Chen, Y.C. Huang, Z.D. Diao, S.Z. Li, L.J. Guo, S. H. Shen, Synergy of dopants and defects in graphitic carbon nitride with exceptionally modulated band structures for efficient photocatalytic oxygen evolution, Adv. Mater. 31 (43) (2019).

[50] P. Zhang, Y.W. Tong, Y. Liu, J.J.M. Vequizo, H.W. Sun, C. Yang, A. Yamakata, F. T. Fan, W. Lin, X.C. Wang, W.Y. Choi, Heteroatom dopants promote two-electron o (2)reduction for photocatalytic production of h(2)o(2)on polymeric carbon nitride, Angew. Chem. Int. Ed. 59 (37) (2020) 16209–16217.

[51] T.T. Hou, H.L. Peng, Y. Xin, S.M. Wang, W.K. Zhu, L.L. Chen, Y. Yao, W.H. Zhang, S.Q. Liang, L.B. Wang, Fe single-atom catalyst for visible-light-driven photofixation of nitrogen sensitized by triphenylphosphine and sodium iodide, ACS Catal. 10 (10) (2020) 5502–5510.

[52] J. Luo, Y.N. Liu, C.Z. Fan, L. Tang, S.J. Yang, M.L. Liu, M.E. Wang, C.Y. Feng, X. L. Ouyang, L.L. Wang, L. Xu, J.J. Wang, M. Yan, Direct attack and indirect transfer mechanisms dominated by reactive oxygen species for photocatalytic h2o2 production on g-c3n4 possessing nitrogen vacancies, ACS Catal. 11 (18) (2021) 11440–11450.

[53] X.J. Bai, T.Q. Jia, X.Y. Wang, S.S. Hou, D. Hao, Bingjie-Ni, High carrier separation efficiency for a defective g-C3N4 with polarization effect and defect engineering: mechanism, properties and prospects, Cat. Sci. Technol. 11 (16) (2021) 5432–5447.

[54] Y. Guo, W.X. Shi, Y.F. Zhu, Internal electric field engineering for steering photogenerated charge separation and enhancing photoactivity, Ecomat 1 (1) (2019).

[55] L. Xu, Q. Li, X.F. Li, M.Q. Long, T. Chen, B.J. Peng, L.L. Wang, Y.W. Yang, C. J. Shuai, Rationally designed 2D/2DSiC/g-C3N4 photocatalysts for hydrogen production, Cat. Sci. Technol. 9 (15) (2019) 3896–3906.

[56] R. Chen, F. Fan, T. Dittrich, C. Li, Imaging photogenerated charge carriers on surfaces and interfaces of photocatalysts with surface photovoltage microscopy, Chem. Soc. Rev. 47 (22) (2018) 8238–8262.

[57] J. Li, L. Cai, J. Shang, Y. Yu, L. Zhang, Giant enhancement of internal electric field boosting bulk charge separation for photocatalysis, Adv. Mater. 28 (21) (2016) 4059–4064.

[58] P. Kumar, E. Vahidzadeh, U.K. Thakur, P. Kar, K.M. Alam, A. Goswami, N. Mahdi, K. Cui, G.M. Bernard, V.K. Michaelis, K. Shankar, C(3)N(5): a low bandgap semiconductor containing an azo-linked carbon nitride framework for photocatalytic, photovoltaic and adsorbent applications, J. Am. Chem. Soc. 141 (13) (2019) 5415–5436.

[59] K.L. Corps, C.W. Schlenker, Ultrafast spectroscopy reveals electron-transfer cascade that improves hydrogen evolution with carbon nitride photocatalysts, J. Am. Chem. Soc. 139 (23) (2017) 7904–7912.

[60] C. Merschjann, T. Tyborski, S. Orthmann, F. Yang, K. Schwarzburg, M. Lublow, M. C. Lux-Steiner, T. Schedel-Niedrig, Photophysics of polymeric carbon nitride: an optical quasimonomer, Phys. Rev. B 87 (20) (2013).

[61] Y.B. Zhao, P. Zhang, Z.C. Yang, L.N. Li, J.Y. Gao, S. Chen, T.F. Xie, C.Z. Diao, S. B. Xi, B.B. Xiao, C. Hu, W.Y. Choi, Mechanistic analysis of multiple processes controlling solar-driven H2O2 synthesis using engineered polymeric carbon nitride, Nat. Commun. 12 (1) (2021).

[62] Z.Z. Lin, X.C. Wang, Nanostructure engineering and doping of conjugated carbon nitride semiconductors for hydrogen photosynthesis, Angew. Chem. Int. Ed. 52 (6) (2013) 1735–1738.

[63] J.R. Ran, T.Y. Ma, G.P. Gao, X.W. Du, S.Z. Qiao, Porous P-doped graphitic carbon nitride nanosheets for synergistically enhanced visible-light photocatalytic H-2 production, Energy Environ. Sci. 8 (12) (2015) 3708–3717.

[64] Y. Di, X. Wang, A. Thomas, M. Antonietti, Making Metal–carbon nitride heterojunctions for improved photocatalytic hydrogen evolution with visible light, ChemCatChem 2 (7) (2010) 834–838.

[65] G.-H. Moon, W. Kim, A.D. Bokare, N.-E. Sung, W. Choi, Solar production of H2O2on reduced graphene oxide–TiO2hybrid photocatalysts consisting of earth-abundant elements only, Energy Environ. Sci. 7 (12) (2014) 4023–4028.

[66] P. Zhang, Y. Tong, Y. Liu, J.J.M. Vequizo, H. Sun, C. Yang, A. Yamakata, F. Fan, W. Lin, X. Wang, W. Choi, Heteroatom dopants promote two-electron o(2) reduction for photocatalytic production of h(2) o(2) on polymeric carbon nitride, Angew. Chem. Int. Ed. Engl. 59 (37) (2020) 16209–16217.

[67] M. Hojamberdiev, R. Vargas, Z.C. Kadirova, K. Kato, H. Sena, A.G. Krasnov, A. Yamakata, K. Teshima, M. Lerch, Unfolding the role of b site-selective doping of aliovalent cations on enhancing sacrificial visible light-induced photocatalytic h-2 and o-2 evolution over BaTaO2N, ACS Catal. 12 (2) (2022) 1403–1414.

[68] H.B. Yu, J.H. Huang, L.B. Jiang, X.Z. Yuan, K.X. Yi, W. Zhang, J. Zhang, H.Y. Chen, Steering photo-excitons towards active sites: Intensified substrates affinity and spatial charge separation for photocatalytic molecular oxygen activation and pollutant removal, Chem. Eng. J. 408 (2021).

[69] Z.S. Chen, S. Zhang, Y. Liu, N.S. Alharbi, S.O. Rabah, S.H. Wang, X.X. Wang, Synthesis and fabrication of g-C3N4-based materials and their application in elimination of pollutants, Sci. Total Environ. 731 (2020).

[70] C. Xia, J.Y. Kim, H.T. Wang, Recommended practice to report selectivity in electrochemical synthesis of H2O2, Nat. Catal. 3 (8) (2020) 605–607.

[71] G.H. Moon, W. Kim, A.D. Bokare, N.E. Sung, W. Choi, Solar production of H2O2 on reduced graphene oxide-TiO2 hybrid photocatalysts consisting of earth-abundant elements only, Energy Environ. Sci. 7 (12) (2014) 4023–4028.

[72] L. Luo, Z.J. Wang, X. Xiang, D.P. Yan, J.H. Ye, Selective activation of benzyl alcohol coupled with photoelectrochemical water oxidation via a radical relay strategy, ACS Catal. 10 (9) (2020) 4906–4913.

[73] Q.Y. Wu, Y. Liu, J.J. Cao, Y. Sun, F. Liao, Y. Liu, H. Huang, M.W. Shao, Z.H. Kang, A function-switchable metal-free photocatalyst for the efficient and selective production of hydrogen and hydrogen peroxide, J. Mater. Chem. A 8 (23) (2020) 11773–11780.

[74] H. Li, P. Wen, D.S. Itanze, Z.D. Hood, S. Adhikari, C. Lu, X. Ma, C.C. Dun, L. Jiang, D.L. Carroll, Y.J. Qiu, S.M. Geyer, Scalable neutral H2O2 electrosynthesis by platinum diphosphide nanocrystals by regulating oxygen reduction reaction pathways, Nat. Commun. 11 (1) (2020).

[75] K. Jiang, J.J. Zhao, H.T. Wang, Catalyst design for electrochemical oxygen reduction toward hydrogen peroxide, Adv. Funct. Mater. 30 (35) (2020).

[76] L.S. Liu, J.H. Huang, H.B. Yu, J. Wan, L.Y. Liu, K.X. Yi, W. Zhang, C.Y. Zhang, Construction of MoO3 nanopaticles /g-C3N4 nanosheets 0D/2D heterojuntion photocatalysts for enhanced photocatalytic degradation of antibiotic pollutant, Chemosphere 282 (2021).

[77] W.H. Zhang, Y.Y. Peng, Y.J. Yang, L. Zhang, Z.Y. Bian, H. Wang, Bismuth-rich strategy intensifies the molecular oxygen activation and internal electrical field for the photocatalytic degradation of tetracycline hydrochloride, Chem. Eng. J. 430 (2022).

[78] Q.S. Chen, H.Q. Zhou, J.C. Wang, J.H. Bi, F. Dong, Activating earth-abundant insulator BaSO4 for visible-light induced degradation of tetracycline, Appl. Catal. B Environ. 307 (2022).